

Cellulose Nanocrystal-Incorporated MAPbI₃ for Inverted Perovskite Solar Cells with Enhanced Efficiency and Stability

Yen-Chung Feng,^{||} Cheng-En Cai,^{||} Bo-Tau Liu, Hongta Yang, and Rong-Ho Lee*Cite This: *ACS Appl. Energy Mater.* 2024, 7, 12092–12102

Read Online

ACCESS |



Metrics & More



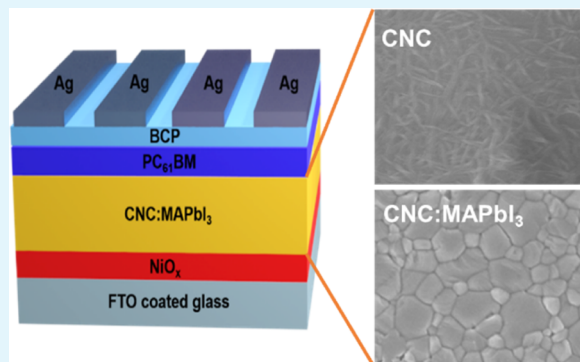
Article Recommendations



Supporting Information

ABSTRACT: Herein, cellulose nanocrystals (CNCs) were added to the MAPbI₃ layer to enhance the photovoltaic properties of MAPbI₃-based inverted perovskite solar cells (PVSCs). The addition of CNCs to the perovskite active layer helps repair crystal defects, improves crystal quality, and stabilizes the perovskite film structure by forming hydrogen bonds between hydroxyl groups and MAPbI₃. This defect passivation by CNCs leads to the formation of larger and denser crystal grains along with enhanced light absorption in the CNC-doped perovskite films. Consequently, trap density is reduced and carrier recombination is suppressed, thereby improving the power conversion efficiency (PCE) and stability of the CNC-doped PVSCs. The structure of the CNC-based inverted PVSCs comprises fluorine-doped tin oxide/NiO_x/CNC:MAPbI₃/PC₆₁BM/BCP/Ag. The CNC-doped PVSC demonstrated an open-circuit voltage (V_{OC}) of 1.07 V, a short-circuit current density (J_{SC}) of 24.43 mA cm⁻², a fill factor (FF) of 76.1%, and a PCE of 19.90%. Furthermore, the insertion of copolyacrylamide (PMD2S) at the interface between the perovskite active layer and the NiO_x-based hole-transport layer effectively reduced the number of interfacial crystal defects. The MAPbI₃ layer deposited on PMD2S-modified NiO_x exhibited denser crystal packing and higher carrier mobility, achieving a V_{OC} of 1.08 V, a J_{SC} of 25.03 mA cm⁻², an FF of 76.7%, and a PCE of 20.72%. Additionally, the CNC-doped PVSC, protected with a hydrophobic electrospun PVDF-HFP film, retained 80% of its initial PCE after storage for 600 h under ambient conditions (30 °C, 50% relative humidity).

KEYWORDS: cellulose nanocrystals, perovskite, MAPbI₃, photovoltaic properties, perovskite solar cells



1. INTRODUCTION

Hybrid organic–inorganic halide perovskite solar cells (PVSCs) have garnered considerable attention due to their excellent optical absorption properties, ambipolar charge transport capabilities, the presence of weakly bound excitons that efficiently dissociate into free charges, and long electron–hole diffusion lengths.^{1–5} Since their initial application in solar cells, achieving a power conversion efficiency (PCE) of 3.8% in 2009, the PCE of PVSCs has increased to 25.7% in just over a decade.^{1–5} PVSCs are classified into two structural categories: mesoporous and planar. Regular PVSCs feature a mesoporous metal-oxide-based electron-transporting layer (ETL), such as SnO₂, onto which the perovskite layer is deposited. This is followed by a Spiro-OMeTAD-based hole-transporting layer (HTL) on top of the perovskite layer.^{6,7} Although regular PVSCs have achieved the highest reported PCEs, the mesoscopic structure of the ETL poses a substantial drawback, as it complicates device fabrication.⁸ By contrast, inverted PVSCs use a planar structure in which a methylammonium lead halide (MAPbI₃)-based perovskite layer is deposited onto an HTL, with a 6,6-phenyl-C60-butyric acid methyl ester (PC₆₁BM)-based ETL applied above the perovskite layer.⁹ These PVSCs are attractive due to their simpler and more cost-

effective fabrication. Moreover, inverted PVSCs with MAPbI₃-based perovskite layers have demonstrated relatively low hysteresis, while maintaining high PCEs and improved stability.¹⁰ However, the presence of interfacial and crystal defects occurring at the perovskite/HTL and ETL/perovskite interfaces, as well as within the perovskite layer, continues to limit the photovoltaic (PV) performance of both regular and inverted PVSCs by promoting nonradiative recombination.^{11–20}

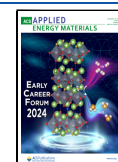
Cellulose, the most abundant and readily accessible biopolymer in nature, is primarily derived from plants.^{21,22} A large number of hydroxyl groups are present on the polymer backbone of cellulose. Commercial cellulose derivatives, including ethyl cellulose, hydroxyethyl cellulose, hydroxypropyl cellulose, cellulose acetate, and cellulose acetate butyrate,^{23–29} have been successfully integrated into the perovskite layers of

Received: October 13, 2024

Revised: December 4, 2024

Accepted: December 4, 2024

Published: December 9, 2024



PVSCs. The hydrogen bonding between the hydroxyl or ester groups of these derivatives and the perovskite material plays a crucial role in passivating charge defect traps at the grain boundaries of the perovskite layer.²³ In addition to passivation, cellulose derivatives act as scaffolds for the perovskite structure, reducing annealing-induced lattice strain during film fabrication and thereby enhancing the PV performance.³⁰ Furthermore, the addition of cellulose derivatives to perovskite films can considerably improve their thermal stability, moisture resistance, and photostability by stabilizing the crystal structure through hydrogen bonding.^{24,25} In addition, cellulose derivatives enhance visible transmittance and considerably improve the thermal stability of MAPbI₃ without adversely affecting the PV performance of PVSCs.²⁶ Quaternary ammonium halide-containing cellulose derivatives have been specifically synthesized as defect passivation additives for MAPbI₃-based inverted PVSCs.³¹ These derivatives repair crystal defects, enhance the crystallinity, and improve the uniformity of the perovskite layer during film formation. Nevertheless, the penetration of polymer long chains among multiple crystal domains in the perovskite layer could affect the stability of the MAPbI₃ crystals. The steric bulk and thermal molecular motion of the polymer backbones in cellulose derivatives lead to a decrease in the average size of the perovskite crystals.³¹ When used as interfacial modifiers between NiO_x and MAPbI₃ layers, quaternary ammonium chloride-containing cellulose derivatives help minimize interfacial defects, enhancing PV performance.³² The hydrophilic polymer chains improve compatibility between NiO_x and perovskite layers, while the quaternary ammonium chloride at the interface passivates defects, strengthens interfacial contact, and increases the crystallinity and stability of the perovskite layer.³³ Ionic and nonionic cellulose derivatives have also been synthesized as eco-friendly additives to promote perovskite growth.³⁴ For example, a cationic cellulose derivative featuring an imidazolium cation and a chloride anion considerably facilitates perovskite crystallization, grain growth, and directional orientation. This process shifts excess PbI₂ to the grain surface or forms plate-like crystallites in localized regions, which suppresses defect formation, reduce grain boundaries, enhance carrier extraction, inhibits nonradiative recombination, and improve both the PV performance and stability of regular PVSCs.³⁴ Moreover, a bifunctional cellulose derivative, carbazole-containing cellulose (C-Cz), has been synthesized with methoxy groups on the backbone and redox-active carbazole side chains for use as an interfacial crystal defect modifier between the Spiro-OMeTAD and perovskite layers.³⁵ This bifunctional material exhibits excellent energy-level alignment, strong thermal stability, and robust interactions with the perovskite surface—features that are critical for efficient carrier transport and defect passivation. Consequently, the incorporation of C-Cz as an interfacial modifier considerably enhances the PCE and the long-term stability of PVSCs. These results underscore the potential of bifunctional cellulose materials as interfacial layers, offering effective charge-transport properties and strong passivation capabilities for efficient and stable regular PVSCs.

Cellulose fibers subjected to acid hydrolysis yield nanoscale rodlike crystalline structures known as cellulose nanocrystals (CNCs).^{36,37} CNCs possess several advantageous properties, including high crystallinity, a large aspect ratio, biodegradability, nanodimensions, lightweight, and an extensive surface area.³⁶ These attributes make CNCs highly promising for diverse applications.^{38–40} However, their use in PVSCs,

compared to cellulose derivatives, has been explored in only a limited number of studies.⁴¹ For instance, cinnamate-functionalized CNCs (Cin-CNCs) have been developed as interfacial modifiers between SnO₂ and the perovskite layer in regular PVSCs. By improving interfacial contact and establishing cascade energy alignment, Cin-CNCs facilitate the desired perovskite film morphology, passivate interfacial crystal defects, and suppress charge recombination at the SnO₂/perovskite interface. These effects enhance carrier transport and crystal quality in the perovskite layer, leading to superior PV performance, along with improved storage and light-soaking stability. Herein, CNCs were incorporated into the MAPbI₃ layer to enhance the PV properties of the MAPbI₃-based PVSCs. The nanoparticle CNC, with a length of approximately 100–300 nm, would not permeate through multiple crystal domains in the perovskite layer or compromise the stability and grain size of the MAPbI₃ crystals.³¹ The device architecture of CNC-based inverted PVSCs consisted of fluorine-doped tin oxide (FTO)/NiO_x/CNC:MAPbI₃/PC61BM/BCP/Ag (Figure 1). The inclusion of CNCs in

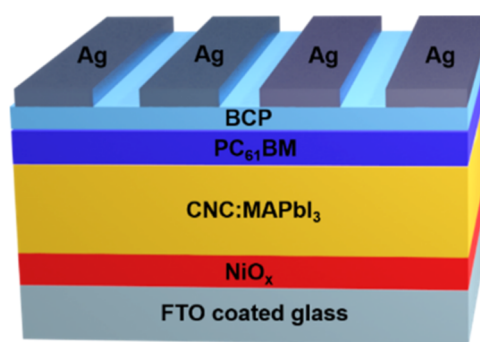


Figure 1. Architecture of the CNC-doped inverted PVSC.

the perovskite active layer is expected to repair crystal defects, improve crystal quality, and stabilize the perovskite film structure by the formation of hydrogen bonds between hydroxyl groups and MAPbI₃. Through defect passivation, CNCs are anticipated to promote the growth of larger and denser crystal grains in the perovskite films thereby reducing trap density and suppress carrier recombination. These improvements are expected to enhance both the PCE and stability of CNC-doped PVSCs. The effects of CNC doping on various properties of MAPbI₃ films in PVSCs were systematically studied, including crystal grain size, X-ray diffraction (XRD) intensity, UV–vis absorption, photoluminescence (PL) intensity, trap density, charge mobility, carrier lifetime, and PV performance. To further optimize the performance of CNC-based PVSCs, a copolyacrylamide (PMD25) layer was introduced at the interface between the perovskite active layer and the NiO_x-based hole-transport layer to reduce the number of interfacial crystal defects. Additionally, a hydrophobic electrospun PVDF-HFP film was deposited on the cathode layer of the CNC-doped PVSCs to enhance device stability under storage conditions.

2. EXPERIMENTAL DETAILS

2.1. Chemicals. CNCs (diameter: 10–20 nm; length: 300–900 nm) were procured from Nanografi Nano Technology and used without further modification. Bathocuproine (BCP) was obtained from Acros. PC₆₁BM was purchased from Uni-Onward and used as received without additional purification. Methylamine (CH₃NH₂),

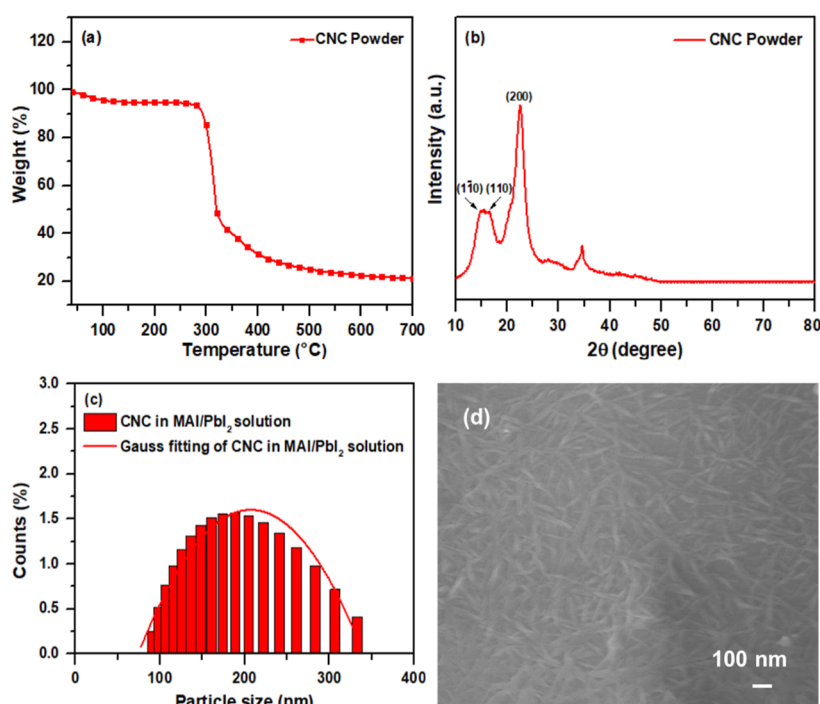


Figure 2. (a) Thermal stability, (b) XRD image morphology, (c) particle size distribution, and (d) SEM image of the CNC powder.

lead iodide (PbI_2), and other chemicals and reagents were sourced from Aldrich, Acros, and TCI Chemical and were used as supplied. Solvents such as *N,N*-dimethylformamide (DMF), dimethyl sulfoxide (DMSO), and chlorobenzene (CB) were freshly distilled over suitable drying agents and purged with N_2 prior to use to ensure their purity. The water-soluble cationic copolyacrylamide (PMD25) was synthesized following the procedure outlined in the literature.⁴² Poly[3-(4-carboxybutyl)thiophene-2,5-diyl] (P3CT, $M_w = 30,000\text{--}40,000\text{ g mol}^{-1}$) was obtained from Rieke Metals. SnO_2 , dispersed in water (15 wt %), was purchased from Alfa Aesar. Poly(vinylidene fluoride-co-hexafluoropropylene) (PVDF-HFP) with a weight-average molecular weight (M_w) of 400,000 g/mol was purchased from Sigma-Aldrich and used without further modification.

2.2. Characterization of CNC-Doped Perovskite Layers. A Horiba FT-720 Fourier transform infrared (FTIR) spectrometer was used to record FTIR spectra. Thermogravimetric analysis (TGA) was conducted using a PerkinElmer Pyris1 system to determine the thermal decomposition temperature (T_d) of the CNC powder, defined as the temperature at which 10% weight loss occurs. The analysis was performed under a nitrogen (N_2) atmosphere at a heating rate of $10\text{ }^\circ\text{C min}^{-1}$. The particle size distribution of CNCs (0.5 mg) in 8 mL of MAI/ PbI_2 -based precursor solution (DMF/DMSO: 4/1, v/v) was measured by using the dynamic light scattering (DLS) method (Litesizer DLS 100). The DLS sample was prepared by stirring the CNC solution at $85\text{ }^\circ\text{C}$ for 2 h. The particle size distribution of CNCs (0.5 mg) in an 8 mL DMF/DMSO (4:1, v/v) solvent mixture was measured using DLS with a Litesizer DLS 100 instrument. The CNC solution was subjected to ultrasonic treatment for 2 h at room temperature before the DLS measurements. The absorption spectra of CNC-doped MAPbI_3 films, coated on both pristine and PMD25-modified NiO_x -deposited FTO glass substrates, were recorded using a Hitachi U3010 UV-vis spectrometer. PL spectra were obtained by using a Hitachi F-4500 fluorescence spectrophotometer. Time-resolved PL (TRPL) spectra of CNC-doped MAPbI_3 films, deposited on pristine and PMD25-modified NiO_x -deposited FTO glass, were recorded using a Horiba Fluoromax-4 spectrometer with a Delta Time TCSPC-MCS kit and a 405 nm pulsed light-emitting diode as the excitation source. For all UV-vis, PL, and TRPL measurements, the CNC-doped MAPbI_3 films were encapsulated with glass sheets to ensure stability during analysis. The

surface morphologies of CNC-doped MAPbI_3 layers were analyzed by using atomic force microscopy (AFM; Seiko SII SPA400) in tapping mode. Surface and cross-sectional morphologies of CNC-doped perovskite layers coated on pristine and PMD25-modified NiO_x layers were characterized by using a cold field emission scanning electron microscopy (SEM) instrument (Hitachi-4800) operated at an acceleration voltage of 1.5–2.0 kV. The crystalline structures of CNC-doped perovskite layers were determined by powder X-ray diffraction (XRD; Shimadzu SD-D1), using a Cu target operated at 35 kV and 30 mA.

2.3. Fabrication and Characterization of PVSCs. The PVSCs herein had a structure of FTO-deposited glass/ NiO_x /CNC/ PC_{61}BM /BCP/Ag (100 nm), with the NiO_x layer modified by PMD25. The FTO-deposited glass (sheet resistance: $7\text{ }\Omega\text{ square}^{-1}$) was purchased from Solaronix. The PVSCs were fabricated as follows: glass substrates with patterned FTO electrodes were thoroughly washed and then cleaned by using the O_2 plasma treatment. The NiO_x precursor solution was prepared by dissolving nickel(II) acetate tetrahydrate (100 mg) in 2-propanol and ethanolamine, stirred at $70\text{ }^\circ\text{C}$, and filtered through a $0.45\text{ }\mu\text{m}$ PTFE filter. A thin NiO_x -based HTL layer was spin-coated onto the FTO substrates, dried at $80\text{ }^\circ\text{C}$ for 10 min, and annealed at $450\text{ }^\circ\text{C}$ for 60 min to achieve a thickness of approximately 10–20 nm. PMD25, dissolved in deionized water (0.1 wt %) and stirred for 24 h, was spin-coated onto the NiO_x layer at 4000 rpm for 1 min and dried at $65\text{ }^\circ\text{C}$ for 1 h to form the PMD25-modified NiO_x layer. The perovskite precursor solution was prepared by dissolving PbI_2 (1290.83 mg) and MAI (445.12 mg) in a DMF/DMSO mixture (4:1, v/v) with CNC (0.3, 0.5, 1.0, or 2.0 mg) added and stirring at $85\text{ }^\circ\text{C}$ for 2 h. The solution was spin-coated onto the HTL-coated substrates at 2000 rpm for 1 min, with $0.4\text{ }\mu\text{L}$ of chlorobenzene (CB) applied as an antisolvent at 40 s before the end of spin-coating. The films were dried at $100\text{ }^\circ\text{C}$ for 10 min and designated as CNC-0.3, CNC-0.5, CNC-1.0, or CNC-2.0 based on the CNC concentration, while the CNC-0.5-based film on the PMD25-modified NiO_x layer was labeled PMD25/CNC-0.5. A PC_{61}BM solution in CB (20 mg mL^{-1}) was spin-coated onto the MAPbI_3 layer at 2000 rpm for 30 s, followed by annealing at $100\text{ }^\circ\text{C}$ for 10 min. A BCP solution (0.3 mL) in isopropyl alcohol (0.5 mg mL^{-1}) was subsequently deposited on the top of the PC_{61}BM layer. BCP was used as the interface buffer layer between PC_{61}BM and Ag

layers to improve the performance of the PVSCs. Finally, the Ag cathode was thermally deposited onto the PC₆₁BM layer in a high-vacuum chamber. The PVSCs had an active area of 0.08 cm². The PV characteristics of the PVSCs were measured by using a programmable electrometer (Keithley 2400) in conjunction with current and voltage sources, under simulated solar light (100 mW cm⁻²) from an AM1.5 solar simulator (NewPort Oriel 96000).

Space-charge-limited current (SCLC) measurements were performed to determine the trap density and charge mobility values of the perovskite film.²⁹ Measuring the hole and electron mobilities in CNC-incorporated MAPbI₃ layers was essential for understanding the additive effects of CNCs on the perovskite layers. The architectures of the hole-only and electron-only devices were FTO/NiO_x or NiO_x/CNC/P3CT/Au and FTO/SnO₂/CNC/PC61BM/Ag, respectively. For the hole-only device, a P3CT-based HTL was coated onto the perovskite layer. P3CT (1.5 mg) was dissolved in chlorobenzene (CB, 1 mL), spin-coated onto the perovskite layer at 4000 rpm for 60 s, and then dried at 100 °C to remove the solvent. Finally, a Ag electrode (90 nm) was deposited by thermal evaporation at a rate of 0.8–1.2 Å s⁻¹. For the electron-only device, a SnO₂-based ETL was coated onto the FTO-deposited glass. A 2.7 wt % SnO₂ gel solution was spin-coated onto the FTO glass at 3000 rpm for 30 s and dried at 150 °C to remove water. The perovskite and PC61BM layers were subsequently coated with the SnO₂ layer. Finally, a gold (Au) electrode (80 nm) was deposited by sputtering.

To enhance device stability, the cathode of the CNC-doped PVSC was encapsulated with a hydrophobic electrospun PVDF-HFP nanofiber film. The PVDF-HFP nanofibers were fabricated via vertical electrospinning of a 20 wt % PVDF-HFP solution in DMF. The electrospinning process was conducted at 14 kV, with a feed rate of 1.4 mL/h and a tip-to-collector distance of 10 cm. The resulting PVDF-HFP membrane-coated devices were dried at 60 °C for 6 h to remove the residual solvent.

3. RESULTS AND DISCUSSION

3.1. Characterization of CNC Nanoparticles. The thermal stability of CNC powder was assessed by using TGA (Figure 2a). The weight loss observed below 150 °C was attributed to the evaporation of water. At temperatures exceeding 300 °C, substantial thermal decomposition of CNC was observed, leading to substantial weight loss and leaving a residual char yield of 21.2%. Cellulose consists of both crystalline and amorphous regions. In the crystalline domains, variations in molecular orientation and hydrogen-bonding networks result in distinct cellulose polymorphs. Four polymorphs of cellulose are known: cellulose I, cellulose II, cellulose III, and cellulose IV.^{36,37} Native cellulose is typically classified as cellulose I.^{36,37} The molecular structure of cellulose I is illustrated in Figure S1. The XRD pattern of CNC powder is shown in Figure 2b, with peaks at 2θ values of approximately 14.5, 16.5, and 22.5°, corresponding to the planes of (110), (110), and (200), respectively. These peaks are consistent with the characteristic diffraction pattern of cellulose I.⁴³ Furthermore, Figure 2c depicts the particle size distribution of CNC in the DMF/DMSO solution, indicating particle sizes ranging from 125 to 325 nm. The SEM image indicated that the width and length of the CNC particles were approximately 10–20 nm and 100–300 nm, respectively. The results indicated that the particle size distribution of CNCs in the DMSO/DMF-based precursor solution did not change significantly compared to that of the CNC powder sample.

3.2. Morphologies of the CNC-Doped Perovskite Films. The impact of CNC as an additive on the crystallization of perovskite films was evaluated by using SEM to examine the morphologies and film quality of MAPbI₃ on the NiO_x layer. This analysis facilitated the identification of optimal processing

conditions for PVSC fabrication. Figure 3a–f presents the top-view SEM images of CNC-doped MAPbI₃ films deposited on

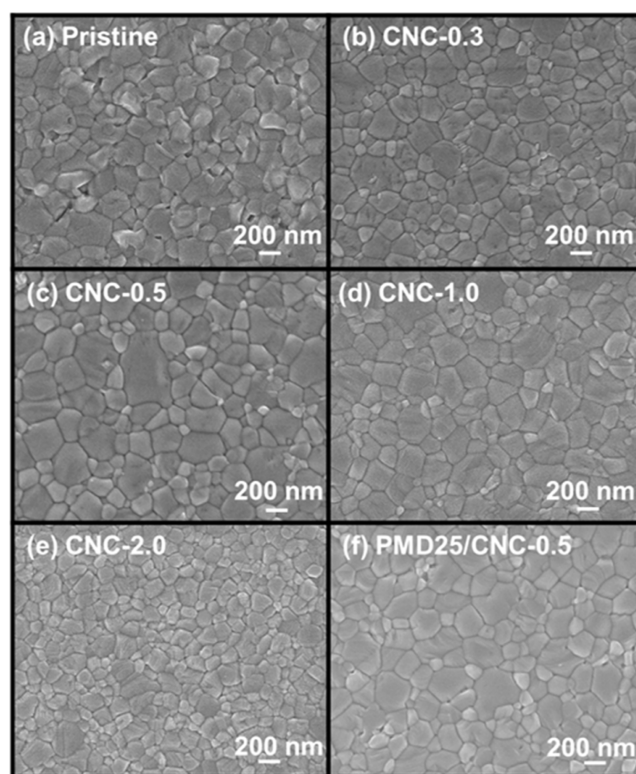


Figure 3. Top-view SEM images of (a) pristine-, (b) CNC-0.3-, (c) CNC-0.5-, (d) CNC-1.0-, (e) CNC-2.0-, and (f) PMD25/CNC-0.5-based perovskite films, recorded after they had been subjected to annealing at 100 °C for 10 min.

pristine and PMD25-modified NiO_x layers. As depicted in Figure 3a, the pristine MAPbI₃ layer exhibited poor film quality in the presence of pinholes. The incorporation of CNC additives into the MAPbI₃ layer, as shown in Figure 3b–d, led to an increase in crystal grain size and the elimination of pinholes. Notably, the crystal grain sizes of the CNC-0.5 and CNC-1.0 layers were larger compared with those of the pristine and CNC-0.3 layers. This improvement is attributed to the hydrogen bonding between the hydroxyl groups of CNC and the perovskite, which reduced the crystal defects in MAPbI₃.^{23–29} The grain sizes of the CNC-0.5 layer were comparable to those of the CNC-1.0 layer. However, an excessive amount of CNC in the MAPbI₃ precursor solution impeded perovskite crystal growth, as demonstrated in Figure 3e, where the grain sizes of the CNC-2.0 layer were smaller than those of the CNC-0.5 and CNC-1.0 layers. Furthermore, the grain sizes of the PMD25/CNC-0.5 layer were similar to those of the CNC-0.5 and CNC-1.0 layers, as illustrated in Figure 3f.

Figure S2a–f illustrates the cross-sectional SEM images of CNC-incorporated MAPbI₃ films deposited on both pristine and PMD25-modified NiO_x layers. The results revealed that the incorporation of CNC into the MAPbI₃ layers increased the layer thickness, indicating that CNC nanoparticles facilitated the crystal growth of the perovskite layer. This increase in thickness enhanced the solar light absorption of the CNC-doped MAPbI₃ films. Among the samples, the CNC-0.5 layer exhibited the greatest thickness (424 nm), followed by

the CNC-1.0 (408 nm) and CNC-0.3 (398 nm) layers. However, excessive CNC in the precursor solution hindered crystal growth, as shown in the CNC-2.0 sample, which displayed a reduced thickness of 377 nm (Figure S2e). Furthermore, the cross-sectional SEM images demonstrated that the film quality of the PMD25/CNC-0.5 layer was considerably superior to that of the CNC-0.5 and CNC-1.0 layers. The thickness of the PMD25/CNC-0.5 layer (452 nm) was notably greater than that of the CNC-0.5 layer (424 nm). This improvement can be attributed to PMD25, which passivated the crystal defects at the interface between the NiO_x and MAPbI₃ layers, thereby enhancing the crystal quality of the perovskite layer.

AFM confirmed the influence of CNC addition on the morphologies of the perovskite films. Figures 4 and S3 display

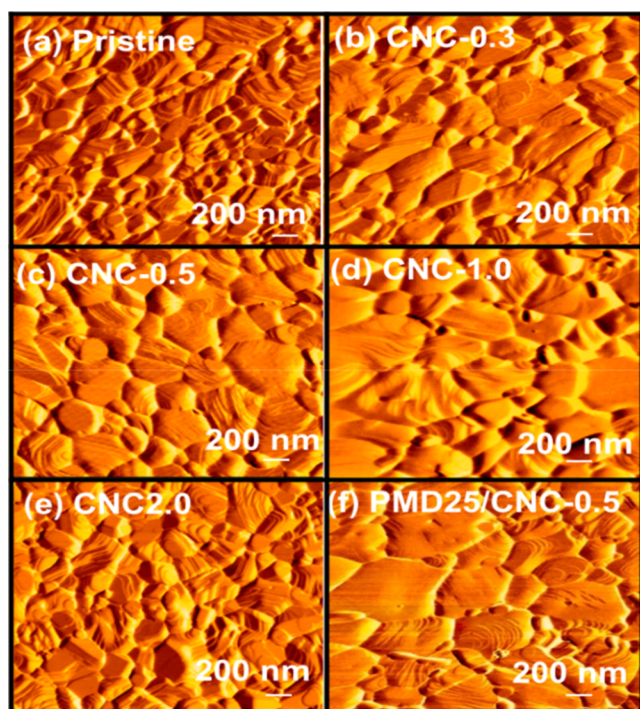


Figure 4. Phase AFM images of CNC-doped perovskite films [(a) pristine-, (b) CNC-0.3-, (c) CNC-0.5-, (d) CNC-1.0-, (e) CNC-2.0-, and (f) PMD25/CNC-0.5-based perovskite films], recorded after they had been subjected to annealing at 100 °C for 10 min.

AFM topographic and phase images of CNC-doped MAPbI₃ films deposited on pristine and PMD25-modified NiO_x layers after annealing at 100 °C for 10 min. The images revealed that the crystal grain size of MAPbI₃ increased with the incorporation of CNC. Specifically, the crystal grain sizes of the CNC-0.5 and CNC-1.0 layers were larger than those of the pristine, CNC-0.3, and CNC-2.0 layers. Moreover, the PMD25/CNC-0.5 layer exhibited slightly larger crystal grain sizes than those of the CNC-0.5 and CNC-1.0 layers. These AFM results were consistent with the SEM observations for the CNC-doped MAPbI₃ films. The average surface roughness values for the pristine, CNC-0.3, CNC-0.5, CNC-1.0, CNC-2.0, and PMD25/CNC-0.5 layers were 7.2, 6.4, 6.3, 6.2, 8.8, and 5.6 nm, respectively. The surface roughness of the CNC-doped perovskite layers decreased with an increasing CNC content. However, an excessive CNC amount, as in the CNC-2.0 layer, was detrimental to reducing the surface roughness.

Notably, the PMD25/CNC-0.5 layer exhibited the lowest surface roughness, surpassing all CNC-doped perovskite layers in smoothness.

3.3. XRD Images and X-ray Photoelectron Spectroscopy Spectra of CNC-Doped Perovskite Films. XRD analysis was conducted to investigate the crystal structures of CNC-incorporated MAPbI₃ films deposited on both pristine and PMD25-modified NiO_x layers (Figure 5). The XRD

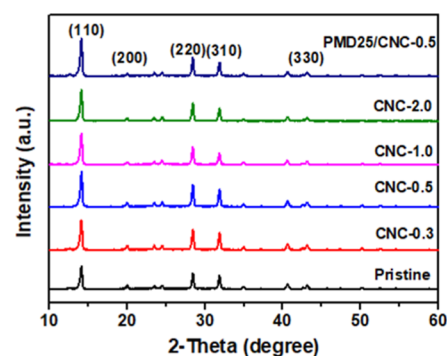


Figure 5. XRD patterns of the CNC-doped perovskite films (pristine, CNC-0.3, CNC-0.5, CNC-1.0, CNC-2.0, and PMD25/CNC-0.5), recorded after they had been subjected to annealing at 100 °C for 10 min.

patterns of the CNC-doped perovskite films revealed typical diffraction peaks of solution-processed MAPbI₃ perovskites at 14.1, 28.4, and 31.86°, corresponding to the (110), (220), and (310) phases, respectively.⁴⁴ These peaks confirmed the formation of tetragonal perovskite structures, with lattice constants *a* and *b* both measuring 8.883 Å and *c* measuring 12.677 Å.⁴⁵ The diffraction peak intensities of the (110), (220), and (310) phases increased with CNC incorporation, indicating an improved crystallinity of the MAPbI₃ films. Among the samples, the CNC-0.5 layer exhibited the highest diffraction intensity, surpassing those of the pristine and other CNC-doped MAPbI₃ samples. Furthermore, the diffraction peak intensities of the PMD25/CNC-0.5 layer were slightly higher than those of the CNC-0.5 and CNC-1.0 layers.

X-ray photoelectron spectroscopy (XPS) was employed to analyze the surface compositions of the CNC-doped MAPbI₃ layers. Figure S4a,c displays the C 1s spectra of the pristine, CNC-0.5, and CNC-2.0 samples. In the deconvoluted C 1s spectrum of the pristine MAPbI₃ film (Figure S4a), two distinct peaks were observed at 283.4 and 284.8 eV, corresponding to the C–C and C–N bonds in amine groups, respectively.³⁴ For the CNC-0.5 and CNC-2.0 samples (Figure S4b,c), an overlap of the C–N and C–OH bonds was identified at 284.8 eV, with the intensity of the C–N/C–OH peak increasing in the CNC-2.0 sample, indicating a higher CNC content.⁴⁶ Furthermore, the Pb 4f spectra of the CNC-0.5 sample exhibited shifts in the binding energies of Pb 4f_{7/2} and Pb 4f_{5/2} toward lower values compared with the pristine MAPbI₃ film (Figure S4d). This shift suggests an interaction between CNC and Pb(II) in the perovskite crystal lattice.⁴⁷ The lone electron pairs in the oxygen atoms of hydroxyl groups within CNC are believed to facilitate defect passivation in the perovskite layer, thereby enhancing the material's quality and stability.⁴⁷

The interaction between CNC and the perovskite was further investigated using FTIR spectroscopy. Figure S5 shows

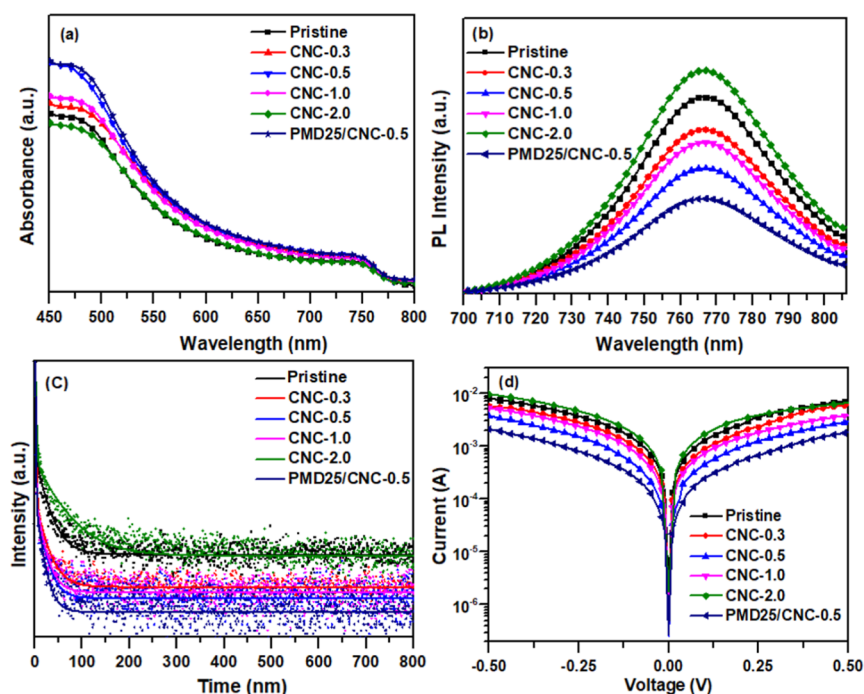


Figure 6. (a) UV–vis spectra, (b) PL spectra, (c) TRPL spectra, and (d) dark-current curves of the CNC-doped MAPbI₃ films deposited on pristine and PMD25-modified NiO_x layers, recorded after they had been subjected to annealing at 100 °C for 10 min.

the FTIR spectra of CNC, MAI, and the CNC/MAI blend (1:1 w/w). The CNC sample exhibited an O–H stretching absorption in the range of 3059–3669 cm⁻¹, along with C–O stretching absorptions at 1058 and 1112 cm⁻¹. Additionally, the absorption peak at 1158 cm⁻¹ corresponds to C–O–C stretching of the glycosidic ring.⁴⁸ For MAI, the N–H stretching band was observed in the range of 2874–3299 cm⁻¹, with N–H bending absorption peaks appearing at 1500–1610 cm⁻¹.⁴⁹ In the CNC/MAI blend, the O–H and N–H stretching bands became broader compared to those of the individual CNC and MAI samples, presumably due to hydrogen-bonding interactions between CNC and MAI.

3.4. UV–Vis Absorption and PL Spectra of CNC-Doped Perovskite Films Deposited on the NiO_x Layers.

UV–vis spectroscopy was used to evaluate the optical properties of CNC-doped MAPbI₃ films deposited on pristine and PMD25-modified NiO_x layers (Figure 6a). The CNC-doped MAPbI₃ films exhibited stronger light absorption across almost the entire spectral range compared to the pristine MAPbI₃ film. Among these, the CNC-0.5 film demonstrated the highest absorption intensity, consistent with its larger crystal grain size and enhanced crystallinity. Interestingly, the absorption intensity of the CNC-2.0 film was slightly lower than that of the pristine MAPbI₃ film, indicating that excessive CNC content may negatively affect the optical performance. Additionally, the PMD25/CNC-0.5 layer exhibited higher absorption intensity than the CNC-0.5 layer, which can be attributed to PMD25's role in effectively passivating crystal defects at the interface between the perovskite and NiO_x layers, further improving light absorption.

To investigate the impact of CNC doping on charge carrier dynamics, we employed PL spectroscopy. As shown in Figure 6b, the PL spectra of the CNC-doped perovskite films exhibited a peak centered at around 768 nm. The reduced PL intensity of the CNC-doped films compared with the pristine MAPbI₃ film suggests enhanced charge carrier

separation. Notably, the CNC-0.5 film exhibited the lowest PL intensity, indicating effective defect passivation. However, excessive CNC doping (e.g., CNC-2.0) led to increased PL intensity, suggesting potential detrimental effects on charge carrier dynamics. Furthermore, the incorporation of PMD25 at the perovskite/NiO_x interface further reduced defect density and improved crystal quality, as evidenced by the lower PL intensity of the PMD25/CNC-0.5 film compared with the CNC-0.5 film.

We recorded TRPL spectra to investigate the influence of the CNC additive on the charge recombination processes of the MAPbI₃ films (Figure 6c). We obtained the carrier lifetime by fitting the PL data to a double-exponential decay model.^{50,51}

$$I(t) = Ae^{-t/\tau_1} + Be^{-t/\tau_2}$$

where A and B are constants and τ_1 and τ_2 are the fast and slow decay constants, respectively. Table S1 summarizes the fitting results for the TRPL spectra. Here, we considered the average lifetime to be the average of the fast and slow decay constants, obtained using the equation

$$\tau_{\text{avg}} = (A\tau_1^2 + B\tau_2^2)/(A\tau_1 + B\tau_2)$$

The constant τ_1 is related to defect recombination or interfacial charge transport from MAPbI₃ to the charge-transport materials; τ_2 is related to radiative recombination.^{50,51} The observed decrease in carrier lifetimes for the CNC-doped MAPbI₃ films relative to the pristine film indicates that the incorporation of CNCs effectively reduces the density of defect states within the perovskite layer. This reduction in defect density enhances the efficiency of charge carrier extraction from the perovskite layer to the respective charge-transport layers, thereby suppressing nonradiative recombination losses. However, an excessive addition of CNC at the MAPbI₃ interface did not lower the number of defects in the MAPbI₃ film, with the CNC-2.0 sample exhibiting a lifetime

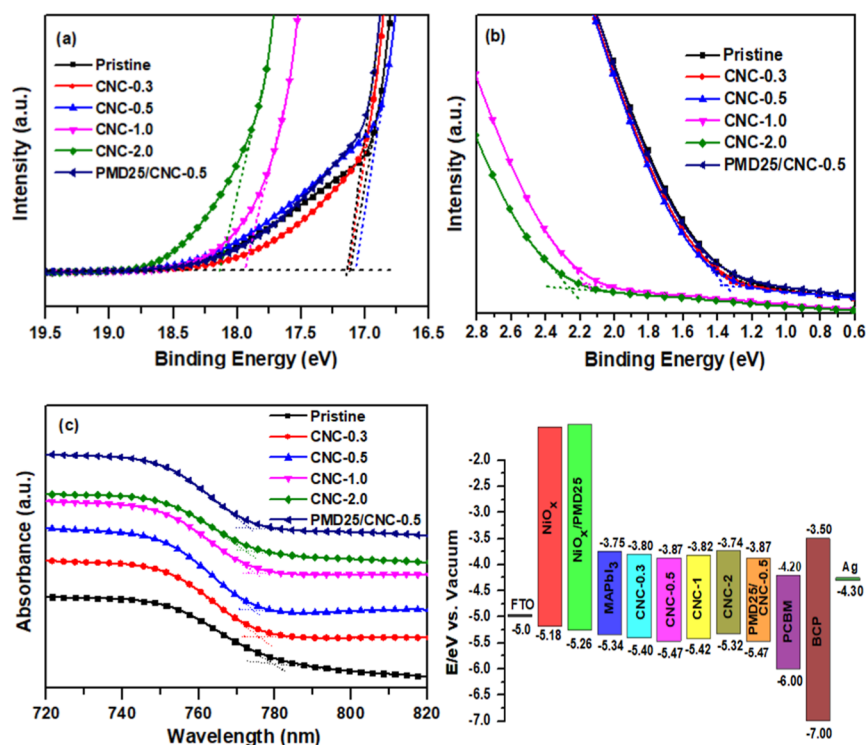


Figure 7. (a) Cutoff region, (b) valence band edge region, (c) UV-vis absorption spectra, and (d) energy-level diagram of the CNC-doped MAPbI₃ films.

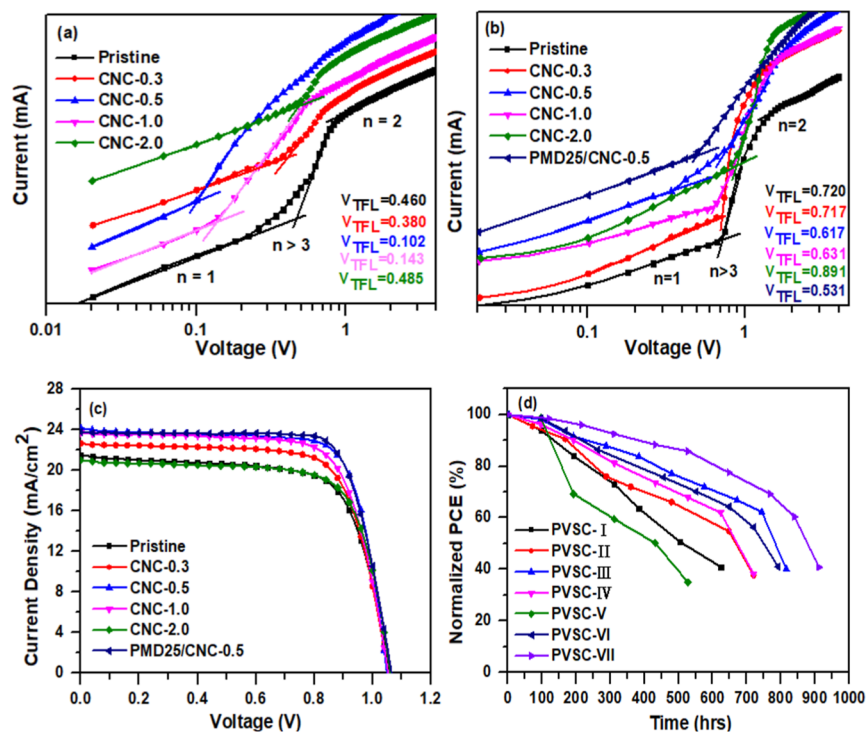


Figure 8. Current density–voltage plots of the (a) electron-only devices (FTO/SnO₂/CNC:MAPbI₃/PC₆₁BM/Ag) and (b) hole-only device (FTO/NiO_x or NiO_x:PMD25/CNC:MAPbI₃/P3CT/Au); (c) current density–voltage characteristics of illuminated (AM 1.5G, 100 mW cm⁻²) PVSCs; (d) storage stability of pristine MAPbI₃, CNC-0.3-, CNC-0.5-, CNC-1.0-, CNC-2.0-, and PMD25/CNC-0.5-based PVSCs.

longer than that of the pristine MAPbI₃ film. Moreover, the lifetimes of the CNC-0.5 films deposited on the PMD25-modified NiO_x layer were shorter than those deposited on the pristine NiO_x layer, which can be attributed to the improved crystal quality of the PMD25/CNC-0.5 sample. Figure 6d

shows the dark-current curves of the CNC-doped MAPbI₃ films deposited on the pristine and PMD25-modified NiO_x layers. The results indicated that the dark current decreased with an increase in the CNC content. The dark-current intensity of CNC-0.5 was significantly lower than those of

CNC-0.3, CNC-1.0, and CNC-2.0. Moreover, the PMD25/CNC-0.5 layer exhibited a lower dark-current intensity than the CNC-0.5 layer, which can be attributed to the superior perovskite film quality of PMD25/CNC-0.5.

3.5. Charge Mobilities and PV Properties of PVSCs Fabricated Using the CNC-Doped Perovskite Layers.

Exploring the energy band structures of the CNC-doped MAPbI₃ films was performed through UPS. The UPS spectra for the cutoff region and the valence band boundary region of CNC-doped MAPbI₃ films are shown in Figure 7a,b. The formulas for calculating the WF and VBM values of CNC-doped MAPbI₃ films are as follows: WF = 21.22 - E_{cutoff} and VBM = WF + E_{onset}, where E_{cutoff} and E_{onset} are identified in Figure 7a,b, respectively.⁵² By analyzing the UV-vis absorption spectra (Figure 7c), the energy band gaps (E_g) of the CNC-doped films were determined. Through the combination of the UV-vis absorption spectra's band gaps, the conduction band minimum (CBM) values of the CNC-doped MAPbI₃ films were established. The UPS spectra were used to summarize the estimated energy-level values of the CNC-doped MAPbI₃ films in Table S2. Moreover, the energy-level diagram for the CNC-doped MAPbI₃ films is shown in Figure 7d. The results indicated that the energy band gap of the MAPbI₃ film changed slightly due to the inclusion of CNC. Compared to the pristine MAPbI₃ film, the CBM and VBM energy levels slightly decreased with increasing CNC content for the CNC-0.3 and CNC-0.5 films. By contrast, the CBM and VBM energy levels increased as the CNC content was further enhanced for the CNC-1.0 and CNC-2.0 samples. Notably, the CBM and VBM energy levels of PMD25/CNC-0.5 were the same as those of CNC-0.5. The lower CBM value favored electron transport from the perovskite layer to the cathode, especially for the CNC-0.5 and PMD25/CNC-0.5 films. Moreover, the lower VBM levels of the CNC-0.5 and PMD25/CNC-0.5-based PVSCs were expected to result in a larger open-circuit voltage (V_{OC}) value.⁵³ Furthermore, a lower VBM value was observed for PMD25-modified NiO_x compared to the pristine NiO_x, which facilitates hole transport from the perovskite layer to the NiO_x layer.

Measuring the trap density and charge mobilities in the CNC-incorporated MAPbI₃ layers is essential for exploring the additive effects of CNC on the perovskite layers. To gain further insights into the charge-transfer mechanism within the photovoltaic solar cells (PVSCs), SCLC analysis was employed to determine the trap-filled limit voltage (V_{TFL}), trap-state density (N_{trap}), and charge mobility via electron-only and hole-only devices. These measurements provide valuable insights into the trap density and charge carrier mobility within the perovskite layer. The electron-only devices employed the structure FTO/SnO₂/CNC:MAPbI₃/PC₆₁BM/Ag, while the hole-only devices utilized the structure FTO/NiO_x or NiO_x:PMD25/CNC:MAPbI₃/P3CT/Au. By analyzing the current density-voltage (J-V) characteristics of these devices, as depicted in Figure 8a,b, the trap-filled limit voltage (VTFL) and trap density (N_{trap}) can be extracted from the log-log plot of the J-V curve. The most common approach to calculating N_{trap} is based on the so-called V_{TFL}^{54,55}

$$N_{\text{trap}} = \frac{2V_{\text{TFL}}\epsilon\epsilon_0}{qL^2}$$

where N_{trap} denotes the trap density, ε₀ denotes the vacuum permittivity (8.854 × 10⁻¹² F m⁻¹), ε denotes the relative

permittivity of MAPbI₃ (32), q denotes elementary charge (1.602 × 10⁻¹⁹ A s), and L denotes the thickness of the MAPbI₃ layer.^{54,55} In Figure 8a, electron-only devices show that the values of V_{TFL} for the pristine, CNC-0.3, CNC-0.5, CNC-1.0, and CNC-2.0 were 0.46, 0.38, 0.10, 0.14, and 0.48 V, corresponding to the electron-trap-state density of 1.01 × 10¹⁶, 7.56 × 10¹⁵, 1.81 × 10¹⁵, 2.79 × 10¹⁵, and 1.08 × 10¹⁶ cm⁻³, respectively. In addition, hole-only devices show that the values of V_{TFL} for the pristine, CNC-0.3, CNC-0.5, CNC-1.0, CNC-2.0, and PMD25/CNC-0.5 were 0.78, 0.72, 0.62, 0.63, 0.89, and 0.52 V, corresponding to the hole-trap-state density of 1.715 × 10¹⁶, 1.44 × 10¹⁶, 1.10 × 10¹⁶, 1.21 × 10¹⁶, 2.79 × 10¹⁶, and 8.09 × 10¹⁵ cm⁻³, respectively (Figure 8b). In the space-charge-limited current regime, the hole and electron mobilities (μ) of the perovskite were determined utilizing the following equation

$$\mu = \frac{8JL^3}{9\epsilon\epsilon_0V^2}$$

where J denotes the current density, V signifies the base voltage, and L signifies the thickness of the MAPbI₃ layer.^{54,55} The electron mobilities of the electron-only devices were estimated as follows: 7.05 × 10⁻³, 7.44 × 10⁻³, 9.12 × 10⁻³, 7.57 × 10⁻³, and 5.65 × 10⁻³ cm² V⁻¹ s⁻¹ for the pristine MAPbI₃-, CNC-0.3-, CNC-0.5-, CNC-1.0-, and CNC-2.0-based devices, respectively. In addition, the hole mobilities of the pristine-, CNC-0.3-, CNC-0.5-, CNC-1.0-, CNC-2.0-, and PMD25/CNC-0.5-based hole-only devices were 3.85 × 10⁻³, 4.08 × 10⁻³, 4.20 × 10⁻³, 3.12 × 10⁻³, and 4.26 × 10⁻³ cm² V⁻¹ s⁻¹, respectively. The SCLC measurements revealed a considerable reduction in both VTFL and N_{trap} with an increase in the CNC concentration, with the lowest values observed for the CNC-0.5 sample. Conversely, the electron and hole mobilities exhibited an increasing trend with a higher CNC content, reaching a maximum for the CNC-0.5 sample. Furthermore, the PMD25/CNC-0.5 device demonstrated an even lower N_{trap} value and higher hole mobility compared to the CNC-0.5 device. These findings indicate that the incorporation of CNCs into the MAPbI₃ layer, particularly at the optimal concentration of 0.5 wt %, effectively passivates defects and improves the crystal quality of the perovskite film. This enhanced morphology leads to improved charge-transport properties, as evidenced by the higher charge carrier mobilities and reduced trap density. The reduction in trap density and the enhancement of charge carrier mobility are expected to contribute to improved charge extraction and suppressed nonradiative recombination, ultimately leading to increased open-circuit voltage (V_{OC}) and PCE, as will be discussed in subsequent sections.

Figures 8c and S6 illustrate the photocurrent density-voltage plots and incident photon-to-current efficiency (IPCE) spectra of the PVSCs made from CNC-doped MAPbI₃ layers. Table S3 summarizes the statistical values for the PV properties of these PVSCs, including V_{OC}, short-circuit current densities (J_{SC}), FFs, and PCEs. The pristine MAPbI₃-based PVSC-I achieved a V_{OC} of 1.07 V, a J_{SC} of 22.62 mA cm⁻², a fill factor (FF) of 72.0%, and a PCE of 17.43%. In contrast to the original PVSC-I, the PV properties (J_{SC}, FF, and PCE) of the CNC-doped MAPbI₃-based PVSCs (PVSC-II-IV) showed considerable improvement. The IPCE spectra confirmed the increase in the J_{SC} values for PVSCs made from CNC-doped MAPbI₃ layers (Figure S5). The IPCEs for the CNC-0.3,

CNC-0.5, and CNC-1.0-based PVSCs exceeded those of PVSC-I based on the pristine MAPbI₃ layer. Notably, CNC-0.5-based PVSC-III exhibited outstanding performance, achieving a V_{OC} of 1.07 V, a J_{SC} of 24.43 mA cm⁻², an FF of 76.1%, and a PCE of 19.90%. These critical J_{SC} and PCE values correspond to the increased crystal grain size, enhanced XRD diffraction intensity, improved UV–vis absorption, and higher charge mobility of the CNC-0.5 perovskite film. Incorporating the optimal amount of CNC into the MAPbI₃ layer facilitated crystal growth and improved the perovskite layer's quality, resulting in effective charge separation, extraction, and increased charge mobility. However, an excessive amount of CNC did not enhance the PV performance of PVSC-V, as its properties based on CNC-2.0 were poorer than those of the pristine MAPbI₃-based PVSC-I. Furthermore, the PV parameters of the PMD25/CNC-0.5-based PVSC-VI were superior to those of the CNC-0.5-based PVSC-III, attributed to better crystal quality, larger absorption intensity, and higher charge mobility of CNC-0.5 deposited on the PMD25-modified NiO_x layer. Moreover, the PV parameters of CNC-0.5/PVDF-HFP-based PVSC-VII were slightly inferior to those of CNC-0.5-based PVSC-III, as PVSC-VII was exposed to the atmosphere and degraded during electrospinning of the PVDF-HFP layer on the cathode (Table S1).

Figure 8d shows the storage stabilities of the PVSCs (PVSC-I, PVSC-II, PVSC-III, PVSC-IV, PVSC-V, and PVSC-VI) based on pristine MAPbI₃, CNC-0.3, CNC-0.5, CNC-1.0, CNC-2.0, and PMD25/CNC-0.5, measured at 30 °C and 40% relative humidity. The PCE stability of the CNC-based PVSCs outperformed that of the pristine MAPbI₃-based PVSC-I, with the exception of the CNC-2.0-based PVSC-V. Furthermore, the PCE stability of the CNC-0.5 based PVSC-III surpassed that of the CNC-0.3- and CNC-1.0-based PVSCs-II and IV, respectively. Notably, CNC-0.5-based PVSC-III demonstrated a lifetime exceeding 800 h without encapsulation. In addition, the stability of the PMD25/CNC-0.5-based PVSC-VI was slightly poorer than that of the CNC-0.5 based PVSC-III. The incorporation of PMD25 at the interface between the NiO_x and MAPbI₃ layers effectively passivated crystal defects and enhanced crystal growth, thereby stabilizing the perovskite crystal structures. However, the water-soluble nature of PMD25 allowed moisture to permeate into the interface between the MAPbI₃ and NiO_x layers, resulting in poorer PCE stability for the PMD25/CNC-0.5 based PVSC-VI. By contrast, the storage stability of the PVDF-HFP-protected PVSC-VII was improved compared to the CNC-0.5-based PVSC-III (Figure 8d). The deposition of a hydrophobic electrospun PVDF-HFP film on the cathode layer of the CNC-doped PVSC effectively prevented the permeation of moisture and oxygen into the perovskite layer from the sides of the device, thus enhancing the storage stability of the PVSC (Figure S7).

4. CONCLUSIONS

CNCs were incorporated into the MAPbI₃ layer as a crystal defect passivation additive to enhance the PV properties of the MAPbI₃-based inverted PVSCs. The crystal defect passivation facilitated by CNCs leads to larger crystal grains, denser crystal packing, and increased light absorption intensity in the CNC-doped perovskite films. These improvements reduce trap density and suppress carrier recombination, resulting in enhanced PCE and improved stability of the CNC-doped PVSCs. Furthermore, the introduction of copolyacrylamide at

the interface between the NiO_x-based hole-transport layer and the perovskite layer minimizes the number of interfacial crystal defects. The MAPbI₃ layer formed on the copolyacrylamide-modified NiO_x layer exhibits a denser crystal packing, higher carrier mobility, and superior PV performance. Moreover, the CNC-doped PVSC exhibited higher storage stability when covered with an electrospun PVDF-HFP film. This hydrophobic electrospun PVDF-HFP film, applied to the cathode layer of the PVSC, acts as a barrier against moisture and oxygen infiltration into the perovskite layer from the device edges, further enhancing the storage stability of the PVSC.

■ ASSOCIATED CONTENT

Supporting Information

The Supporting Information is available free of charge at <https://pubs.acs.org/doi/10.1021/acsaem.4c02602>.

Cross-sectional SEM images of CNC-doped MAPbI₃ layers; 3D topographic AFM images of CNC-doped perovskite films; XPS spectra of CNC-doped perovskite film; IPCE spectra of PVSCs; fitted parameters of the TRPL spectra; energy levels of the CNC-doped MAPbI₃ films; and PV performance data of PVSCs (PDF)

■ AUTHOR INFORMATION

Corresponding Author

Rong-Ho Lee – Department of Chemical Engineering, National Chung Hsing University, Taichung 402 Taiwan, Republic of China; Department of Chemical Engineering and Materials Science, Yuan Ze University, Taoyuan City 320, Taiwan; orcid.org/0000-0002-1373-9360; Phone: +886-4-22854308; Email: rhl@dragon.nchu.edu.tw; Fax: +886-4-22854734

Authors

Yen-Chung Feng – Department of Chemical Engineering, National Chung Hsing University, Taichung 402 Taiwan, Republic of China

Cheng-En Cai – Department of Chemical Engineering, National Chung Hsing University, Taichung 402 Taiwan, Republic of China

Bo-Tau Liu – Department of Chemical and Materials Engineering, National Yunlin University of Science and Technology, Yunlin 64002 Taiwan, Republic of China; orcid.org/0000-0002-4087-5739

Hongta Yang – Department of Chemical Engineering, National Chung Hsing University, Taichung 402 Taiwan, Republic of China

Complete contact information is available at: <https://pubs.acs.org/doi/10.1021/acsaem.4c02602>

Author Contributions

Y.-C.F. and C.-E.C. contributed equally to this work. Conceptualization, R.H.L.; data curation, Y.C.F. and C.E.C. writing—original draft preparation, R.H.L.; writing—review and editing, B.T.L. and H.Y.; visualization, H.Y. and R.H.L.; supervision, R.H.L.; project administration, funding acquisition, R.H.L. All authors have read and agreed to the published version of the manuscript.

Notes

The authors declare no competing financial interest.

ACKNOWLEDGMENTS

The authors thank the National Science and Technology Council (NSTC) of Taiwan (grant no. NSTC 113-2221-E-005-006) for financial support.

REFERENCES

- (1) Kojima, A.; Teshima, K.; Shirai, Y.; Miyasaka, T. Organometal halide perovskites as visible-light sensitizers for photovoltaic cells. *J. Am. Chem. Soc.* **2009**, *131*, 6050–6051.
- (2) Chen, J.; Yang, Y.; Dong, H.; Li, J.; Zhu, X.; Xu, J.; Pan, F.; Yuan, F.; Dai, J.; Jiao, B.; Hou, X.; Jen, A. K. Y.; Wu, Z. Highly efficient and stable perovskite solar cells enabled by low-dimensional perovskitoids. *Sci. Adv.* **2022**, *8*, No. eabk2722.
- (3) Chen, J.; Dong, H.; Li, J.; Zhu, X.; Xu, J.; Pan, F.; Xu, R.; Xi, J.; Jiao, B.; Hou, X.; Wei, N. G.; Wang, S. P.; Wu, Z. Solar cell efficiency exceeding 25% through R_b -based perovskitoid scaffold stabilizing the buried perovskite surface. *ACS Energy Lett.* **2022**, *7*, 3685–3694.
- (4) Liu, S.; Biju, V. P.; Qi, Y.; Chen, W.; Liu, Z. Recent progress in the development of high-efficiency inverted perovskite solar cells. *NPG Asia Mater.* **2023**, *15*, 27.
- (5) Nyiekaka, E. A.; Aika, T. A.; Orukpe, P. E.; Akhabe, C. E.; Danladi, E. Development on inverted perovskite solar cells: a review. *Heliyon* **2024**, *10*, No. e24689.
- (6) Wu, P.; Wang, S.; Li, X.; Zhang, F. Advances in SnO_2 -based perovskite solar cells: from preparation to photovoltaic applications. *J. Mater. Chem. A* **2021**, *9*, 19554–19588.
- (7) Liu, B. T.; Huang, Y. S.; Chen, I. R.; Lee, R. H.; Rathinam, B. Pinhole patching by free radicals for highly efficient perovskite solar cells fabricated in high-moisture environments. *ACS Appl. Energy Mater.* **2024**, *7*, 2189–2196.
- (8) Uddin, A.; Yi, H. Progress and challenges of SnO_2 electron transport layer for perovskite solar cells: a critical review. *Sol. RRL* **2022**, *6*, 2100983.
- (9) Li, M.; Yue, Z.; Ye, Z.; Li, H.; Luo, H.; Yang, Q. D.; Zhou, Y.; Huo, Y.; Cheng, Y. Improving the efficiency and stability of MAPbI_3 perovskite solar cells by dipeptide molecules. *Small* **2024**, *20*, 2311400.
- (10) Seo, Y. H.; Cho, I. H.; Na, S. I. Investigation of sol-gel and nanoparticle-based NiO_x hole transporting layer for high-performance planar perovskite solar cells. *J. Alloys Compd.* **2019**, *797*, 1018–1024.
- (11) Zhang, Y.; Kong, T.; Xie, H.; Song, J.; Li, Y.; Ai, Y.; Han, Y.; Bi, D. Molecularly tailored SnO_2 /perovskite interface enabling efficient and stable FAPbI_3 solar cells. *ACS Energy Lett.* **2022**, *7*, 929–938.
- (12) Gong, J.; Cui, Y.; Li, F.; Liu, M. Progress in surface modification of SnO_2 electron transport layers for stable perovskite solar cells. *Small Sci.* **2023**, *3*, 2200108.
- (13) Yang, D.; Yang, R.; Wang, K.; Wu, C.; Zhu, X.; Feng, J.; Ren, X.; Fang, G.; Priya, S.; Liu, S. High efficiency planar-type perovskite solar cells with negligible hysteresis using EDTA-complexed SnO_2 . *Nat. Commun.* **2018**, *9*, 3239.
- (14) Li, F.; Yuan, J.; Ling, X.; Zhang, Y.; Yang, Y.; Cheung, S. H.; Ho, C. H. Y.; Gao, X.; Ma, W. A universal strategy to utilize polymeric semiconductors for perovskite solar cells with enhanced efficiency and longevity. *Adv. Funct. Mater.* **2018**, *28*, 1706377.
- (15) Frolova, L. A.; Davlethanov, A. I.; Dremova, N. N.; Zhidkov, I.; Akbulatov, A. F.; Kurmaev, E. Z.; Aldoshin, S. M.; Stevenson, K. J.; Troshin, P. A. Efficient and stable MAPbI_3 -based perovskite solar cells using polyvinylcarbazole passivation. *J. Phys. Chem. Lett.* **2020**, *11*, 6772–6778.
- (16) Pu, X.; Zhao, J.; Li, Y.; Zhang, Y.; Loi, H. L.; Wang, T.; Chen, H.; He, X.; Yang, J.; Ma, X.; Li, X.; Cao, Q. Stable NiO_x -based inverted perovskite solar cells achieved by passivation of multifunctional star polymer. *Nano Energy* **2023**, *112*, 108506.
- (17) Du, Y.; Xin, C.; Huang, W.; Shi, B.; Ding, Y.; Wei, C.; Zhao, Y.; Li, Y.; Zhang, X. Polymeric surface modification of NiO_x -based inverted planar perovskite solar cells with enhanced performance. *ACS Sustainable Chem. Eng.* **2018**, *6*, 16806–16812.
- (18) Fu, L.; Li, H.; Wang, L.; Yin, R.; Li, B.; Yin, L. Defect passivation strategies in perovskites for an enhanced photovoltaic performance. *Energy Environ. Sci.* **2020**, *13*, 4017–4056.
- (19) Zhang, H.; Pfeifer, L.; Zakeeruddin, S. M.; Chu, J.; Grätzel, M. Tailoring passivators for highly efficient and stable perovskite solar cells. *Nat. Rev. Chem.* **2023**, *7*, 632–652.
- (20) Wang, Y.; Yang, Y.; Uhlík, F.; Slanina, Z.; Han, D.; Yang, Q.; Yuan, Q.; Yang, Y.; Zhou, D. Y.; Feng, L. Enhancing photovoltaic performance of inverted perovskite solar cells via imidazole and benzoimidazole doping of PC_{61}BM electron transport layer. *Org. Electron.* **2020**, *78*, 105573.
- (21) Jyothibasu, J. P.; Lee, R. H. Facile, scalable, eco-friendly fabrication of high-performance flexible all-solid-state supercapacitors. *Polymers* **2018**, *10*, 1247.
- (22) Jyothibasu, J. P.; Kuo, D. W.; Lee, R. H. Flexible and freestanding electrodes based on polypyrrole/carbon nanotube/cellulose composites for supercapacitor application. *Cellulose* **2019**, *26*, 4495–4513.
- (23) Yang, J.; Xiong, S.; Qu, T.; Zhang, Y.; He, X.; Guo, X.; Zhao, Q.; Braun, S.; Chen, J.; Xu, J.; Li, Y.; et al. Extremely low-cost and green cellulose passivating perovskites for stable and high-performance solar cells. *ACS Appl. Mater. Interfaces* **2019**, *11*, 13491–13498.
- (24) He, J.; Ng, C. F.; Young Wong, K.; Liu, W.; Chen, T. Photostability and moisture stability of $\text{CH}_3\text{NH}_3\text{PbI}_3$ -based solar cells by ethyl cellulose. *ChemPlusChem* **2016**, *81*, 1292–1298.
- (25) Zhang, P.; Gu, N.; Song, L.; Chen, W. H.; Du, P.; Yin, X.; Xiong, J. Bifunctional green cellulose derivatives employed for high efficiency and stable perovskite solar cells under ambient environment. *J. Alloys Compd.* **2021**, *886*, 161247.
- (26) Bisconti, F.; Giuri, A.; Dominici, L.; Carallo, S.; Quadri, E.; Po', R.; Biagini, P.; Listorti, A.; Corcione, C. E.; Colella, S.; et al. Managing transparency through polymer/perovskite blending: a route toward thermostable and highly efficient, semi-transparent solar cells. *Nano Energy* **2021**, *89*, 106406.
- (27) Zhu, X.; Lin, R.; Gu, H.; Hu, H.; Liu, Z.; Xing, G.; Wu, Y.; Ouyang, X. Ecofriendly hydroxyalkyl cellulose additives for efficient and stable MAPbI_3 -based inverted perovskite solar cells. *Energy Environ. Mater.* **2023**, *6*, No. e12426.
- (28) Liu, J.; He, Q.; Bi, J.; Lei, M.; Zhang, W.; Wang, G. Remarkable quality improvement of CsPbI_2Br perovskite film by cellulose acetate addition for efficient and stable carbon-based inorganic perovskite solar cells. *Chem. Eng. J.* **2021**, *424*, 130324.
- (29) Xiao, B.; Qian, Y.; Li, X.; Tao, Y.; Yi, Z.; Jiang, Q.; Luo, Y.; Yang, J. Enhancing the stability of planar perovskite solar cells by green and inexpensive cellulose acetate butyrate. *J. Energy Chem.* **2023**, *76*, 259–265.
- (30) Chu, H. Y.; Hong, J. Y.; Huang, C. F.; Wu, J. Y.; Wang, T. L.; Wu, T. M.; Lee, R. H. Enhanced photovoltaic properties of perovskite solar cells by the addition of cellulose derivatives to MAPbI_3 based photoactive layer. *Cellulose* **2019**, *26*, 9229–9239.
- (31) Du, C. S.; Ho, I. H.; Huang, Y. J.; Lee, R. H. Quaternary ammonium halide-containing cellulose derivatives for defect passivation in MAPbI_3 -based perovskite solar cells. *Sustain. Energy Fuels* **2022**, *6*, 3349–3362.
- (32) Ho, I. H.; Huang, Y. J.; Cai, C. E.; Liu, B. T.; Wu, T. M.; Lee, R. H. Enhanced photovoltaic performance of inverted perovskite solar cells through surface modification of a NiO_x -based hole-transporting layer with quaternary ammonium halide-containing cellulose derivatives. *Polymers* **2023**, *15*, 437.
- (33) Liu, Y.; Duan, J.; Zhang, J.; Huang, S.; Ou-Yang, W.; Bao, Q.; Sun, Z.; Chen, X. High efficiency and stability of inverted perovskite solar cells using phenethyl ammonium iodide-modified interface of NiO_x and perovskite layers. *ACS Appl. Mater. Interfaces* **2020**, *12*, 771–779.
- (34) Wang, Y.; Cheng, Y.; Yin, C.; Zhang, J.; You, J.; Wang, J.; Wang, J.; Zhang, J. Manipulating crystal growth and secondary phase PbI_2 to enable efficient and stable perovskite solar cells with natural additives. *Nano-Micro Lett.* **2024**, *16*, 183.

- (35) Zhang, Z.; Wang, C.; Li, F.; Liang, L.; Huang, L.; Chen, L.; Ni, Y.; Gao, P.; Wu, H. Bifunctional cellulose interlayer enabled efficient perovskite solar cells with simultaneously enhanced efficiency and stability. *Adv. Sci.* **2023**, *10*, 2207202.
- (36) Gong, J.; Li, J.; Xu, J.; Xiang, Z.; Mo, L. Research on cellulose nanocrystals produced from cellulose sources with various polymorphs. *RSC Adv.* **2017**, *7*, 33486–33493.
- (37) Nagarajan, S.; Skillen, N. C.; Irvine, J. T. S.; Lawton, L. A.; Robertson, P. K. J. Cellulose II as bioethanol feedstock and its advantages over native cellulose. *Renew. Sustain. Energy Rev.* **2017**, *77*, 182–192.
- (38) Li, W.; Yue, J.; Liu, S. Preparation of nanocrystalline cellulose via ultrasound and its reinforcement capability for poly(vinyl alcohol) composites. *Ultrason. Sonochem.* **2012**, *19*, 479–485.
- (39) Cherhal, F.; Cousin, F.; Capron, I. Structural description of the interface of pickering emulsions stabilized by cellulose nanocrystals. *Biomacromolecules* **2016**, *17*, 496–502.
- (40) Shin, Y.; Exarhos, G. J. Template synthesis of porous titania using cellulose nanocrystals. *Mater. Lett.* **2007**, *61*, 2594–2597.
- (41) Liu, J.; Liu, N.; Li, G.; Wang, Y.; Wang, Z.; Zhang, Z.; Xu, D.; Jiang, Y.; Gao, X.; Lu, X.; Feng, S. P.; Zhou, G.; Liu, J. M.; Gao, J. Cinnamate-functionalized cellulose nanocrystals as interfacial layers for efficient and stable perovskite solar cells. *ACS Appl. Mater. Interfaces* **2023**, *15*, 1348–1357.
- (42) Huang, Y. J.; Cai, C. E.; Feng, Y. C.; Liu, B. T.; Lee, R. H. Water-soluble cationic copolyacrylamides modifying NiO_x for high-performance inverted perovskite solar cells. *ACS Appl. Polym. Mater.* **2023**, *5*, 8949–8959.
- (43) French, A. D. Idealized powder diffraction patterns for cellulose polymorphs. *Cellulose* **2014**, *21*, 885–896.
- (44) Xiao, M.; Huang, F.; Huang, W.; Dkhissi, Y.; Zhu, Y.; Etheridge, J.; Gray-Weale, A.; Bach, U.; Cheng, Y. B.; Spiccia, L. A fast deposition-crystallization procedure for highly efficient lead iodide perovskite thin-film solar cells. *Angew. Chem., Int. Ed. Engl.* **2014**, *53*, 9898–9903.
- (45) Song, Z.; Watthage, S. C.; Phillips, A. B.; Tompkins, B. L.; Ellingson, R. J.; Heben, M. J. Impact of processing temperature and composition on the formation of methylammonium lead iodide perovskites. *Chem. Mater.* **2015**, *27*, 4612–4619.
- (46) Rocks, C.; Svrcek, V.; Maguire, P.; Mariotti, D. Understanding surface chemistry during MAPbI₃ spray deposition and its effect on photovoltaic performance. *J. Mater. Chem. C* **2017**, *5*, 902–916.
- (47) Tan, S.; Huang, T.; Yavuz, I.; Wang, R.; Weber, M. H.; Zhao, Y.; Abdelsamie, M.; Liao, M. E.; Wang, H. C.; Huynh, K.; Wei, K. H.; Xue, J.; Babbe, F.; Goorsky, M. S.; Lee, J. W.; Sutter-Fella, C. M.; Yang, Y. Surface reconstruction of halide perovskites during post-treatment. *J. Am. Chem. Soc.* **2021**, *143*, 6781–6786.
- (48) Rana, M. S.; Rahim, M. A.; Mosharraf, M. P.; Tipu, M. F. K.; Chowdhury, J. A.; Haque, M. R.; Kabir, S.; Amran, M. S.; Chowdhury, A. A. Morphological spectroscopic and thermal analysis of cellulose nanocrystals extracted from waste jute fiber by acid hydrolysis. *Polymers* **2023**, *15*, 1530.
- (49) Harding, A. J.; Dobson, K. D.; Ogunnaike, B. A.; Shafarman, W. N. Thermal and structural characterization of methylammonium- and formamidinium-halide salts. *Phys. Status Solidi A* **2021**, *218*, 2100246.
- (50) Dubey, A.; Adhikari, N.; Mabrouk, S.; Wu, F.; Chen, K.; Yang, S.; Qiao, Q. A strategic review on processing routes towards highly efficient perovskite solar cells. *J. Mater. Chem. A* **2018**, *6*, 2406–2431.
- (51) Li, X.; Liu, X.; Wang, X.; Zhao, L.; Jiu, T.; Fang, J. Polyelectrolyte based hole-transporting materials for high performance solution processed planar perovskite solar cells. *J. Mater. Chem. A* **2015**, *3*, 15024–15029.
- (52) Li, B.; Zhang, C.; Gao, D.; Sun, X.; Zhang, S.; Li, Z.; Gong, J.; Li, S.; Zhu, Z. Suppressing oxidation at perovskite-NiO_x interface for efficient and stable tin perovskite solar cells. *Adv. Mater.* **2024**, *36*, 2309768.
- (53) Liu, B. T.; Zhang, Y. Z.; Zuo, Y. Y.; Rachmawati, D. Passivation and energy-level change of the SnO₂ electron transport layer by reactive titania for perovskite solar cells. *J. Alloys Compd.* **2022**, *929*, 167349.
- (54) Sajedi Alvar, M.; Blom, P. W.; Wetzelaer, G. J. A. Space-charge-limited electron and hole currents in hybrid organic–inorganic perovskites. *Nat. Commun.* **2020**, *11*, 4023.
- (55) Le Corre, V. M.; Duijnste, E. A.; El Tambouli, O.; Ball, J. M.; Snaith, H. J.; Lim, J.; Koster, L. J. A. Revealing charge carrier mobility and defect densities in metal halide perovskites via space-charge-limited current measurements. *ACS Energy Lett.* **2021**, *6*, 1087–1094.